DOI: 10.1002/cphc.200600781

Scanning Tunneling Microscopy and Spectroscopy Studies of 4-Methyl-4′-(*n*-mercaptoalkyl)biphenyls on Au(111)-(1×1)

Gujin J. Su,[a] Rocio Aguilar-Sanchez,[a] Zhihai Li,[a] Ilya Pobelov,[a] Melanie Homberger,[b] Ulrich Simon,[b] and Thomas Wandlowski*[a]

4-Methyl-4′-(n-mercaptoalkyl)biphenyl (CH_3–C_6H_4–C_6H_4–$(CH_2)_n$–SH, n = 3–6, BPn) monolayers assembled on Au(111)-(1×1) in 1,3,5,-trimethylbenzene (TMB) at various temperatures are studied by scanning tunneling microscopy (STM) and scanning tunneling spectroscopy (STS). High resolution STM images reveal that BP3 and BP5 form a ($\sqrt{3}\times 2\sqrt{3}$) repeating motif superimposed on a temperature-dependent Moire pattern. BP4 and BP6 adlayers are characterized by a coexisting ($2\sqrt{3}\times 5\sqrt{3}$) majority phase and a temperature-dependent ($3\times p\sqrt{3}$) minority phase. Assembly at 60 °C or 90 °C leads to p = 5. Compression of the adlayer was found at higher temperatures. Combined with high-resolution structure experiments, the electronic characteristics of BP3 and BP4 self-assembled monolayers (SAMs) were studied by monitoring current–distance (i_T–Δz) and current–voltage (i_T–E_{bias}) characteristics in TMB employing a gold STM tip | BPn | Au(111)-(1×1) configuration. The semilogarithmic (i_T–Δz) plots yielded three linear regions in the range 10 pA ≤ i_T ≤ 20 μA, which were attributed to the different positions of the STM tip with respect to the molecular adlayer (I outside, II in contact with and/or within the adlayer, and III just before the formation of Au–Au nanocontacts). The effective decay constants κ_{eff} and the corresponding barrier heights ϕ_{eff} decrease with decreasing tip–substrate distance. The i_T–E_{bias} curves at low bias voltages are represented by the Simmons tunneling model. Based on measurements in the high current limit, the electric field strength of the dielectric breakdown was estimated to range between $|0.85\pm0.05|\times10^9\ V\,m^{-1}$ and $|1.5\pm0.1|\times10^9\ V\,m^{-1}$.

1. Introduction

The rational design of functional organic | inorganic nanostructures represents a challenging area of current research.[1] Self-assembly is a particular fascinating bottom-up approach to fabricate complex objects and systems (2D arrays and 3D networks) from carefully designed individual building blocks, such as tailored molecules,[2] clusters,[3] and aggregate structures.[4] The idea that ordered monomolecular adlayers on solid substrates can be prepared by self-assembly of custom-synthesized molecules was first demonstrated by Zisman and coworkers.[5] Milestones were the preparation of stable self-assembled monolayers (SAMs[6,7]) from alkyltrichlorosilane on silicon dioxide[8] and from alkanethiols on gold.[9] Thiol-based SAMs are composed of one or two sulfur anchor groups, custom-designed alkyl or phenyl spacer units, and, in some cases, incorporated tailored functionalities.[6,7,9–13] The application of SAMs covers diverse areas such as adhesion,[14] lubrication,[15] microfabrication,[12,16] bioenergetics and biosensors,[17] corrosion,[18] fundamental electrochemistry,[19] and metal deposition[20] as well as the emerging field of nanoelectronics.[21–23] Of particular interest is their ability to control charge transfer in metal | molecular hybrid systems.[24,25]

While most fundamental studies on structure, electrical, and electrochemical properties of organosulfur compounds focused on aliphatic thiols assembled on various gold surfaces in solution or under ultrahigh vacuum (UHV) conditions,[6,7,9–11,19,21–31] aromatic thiols have been investigated far less.[7,13,30,32–34] However, the vision of molecular-level electronics recently triggered considerable interest in aromatic thiol-based molecular rods and functional building blocks composed of single molecules and tailored ensembles, taking advantage of their high conductivity and nonlinear optical properties.[22,23,29–31,33–37] The rigid aromatic system offers unique control of structures and local molecular functionality. Characterizing the order and packing of conjugated arenethiol SAMs is essential for understanding the electronic and optical properties of materials and potential future devices based on them. By employing scanning tunneling microscopy (STM) in air and under UHV conditions, systematic structure studies have been carried out for oligophenlyalkanthiols containing phenyl (Ph),[30] biphenyl (BP*n*),[38–43] or terphenyl (TP*n*)[44–46] backbones

[a] Dr. G. J. Su, Dr. R. Aguilar-Sanchez, Z. Li, I. Pobelov, Priv.-Doz. Dr. T. Wandlowski
Institute of Bio- and Nanosystems (IBN3)
and
Center of Nanoelectronic Systems for Information Technology (CNI)
Research Center Jülich, 52425 Jülich (Germany)
Fax: (+49) 2461-61-3907
E-mail: th.wandlowski@fz-juelich.de

[b] Dr. M. Homberger, Prof. Dr. U. Simon
Institute of Inorganic Chemistry
RWTH Aachen, 52074 Aachen (Germany)

on Au(111) surfaces. The length n of the alkyl spacer varies between 0 and 6. The low-coverage adlayers of these SAMs exhibit a disordered or striped pattern.[30,39] Distinct ordered adlayers were found at high coverages, which were assigned to commensurate $(\sqrt{3}\times\sqrt{3})$,[38] $(2\sqrt{3}\times\sqrt{3})$, $(n\sqrt{3}\times3)$,[39–46] and more complex superstructures.[41,46] Common to all proposed structure models is a herringbone-like packing of the aromatic moiety. Based on a series of spectroscopic[46–49] and STM studies[40–42,46] under UHV conditions and in air, Wöll, Buck, Zharnikov, and their co-workers reported a pronounced odd–even effect dependening on the lengths of the alkyl spacer group with a denser molecular packing for BPn and TPn with n = odd [unit cell: $(\sqrt{3}\times2\sqrt{3})$], in comparison to the less dense packing with n = even [unit cell: $(n\sqrt{3}\times3)$ and more complex].[40–42,46]

Electronic transport properties in metal|molecule|metal junctions with aromatic thiols having one or two anchor groups were carried out by various scanning probe microscopy (SPM) techniques such as STM/STS (STS = scanning tunneling spectroscopy),[21,30,44,50–54] conductive probe atomic force microscopy (CP-AFM)[55,56] and a tuning-fork set-up.[57] Alternative approaches are based on mechanically controlled break junctions,[36] nanopore[58] or electromigration techniques,[59] cross wire junctions,[60] or on a molecular layer sandwiched between two solid metal films,[61] mercury drops,[29] or assembled in magnetic bead junctions.[62] These studies revealed the strong dependence of electron transport properties on the chemical nature of the molecules. They also indicate the importance of combining experiments on local functionality, such as electron transport or recognition, with high-resolution studies on adlayer structures.

Herein, we present the first high-resolution STM study of 4-methyl-4′-(n-mercaptoalkyl)biphenyl (CH_3–C_6H_4–C_6H_4–$(CH_2)_n$–SH, n = 3–6; BPn) monolayers assembled on Au(111)-(1×1) electrode surfaces in combination with local STS experiments in 1,3,5,-trimethylbenzene (TMB) employing a vertical Au|BPn|Au configuration. The project complements our previous electrochemical investigations.[43] The combination of STM and STS provides direct access to electronic properties of the adlayers under strict structure control in a well-defined environment.

The paper is organized as follows: Experimental details are summarized in the next section. We then report on the steady-state and temperature-dependent properties of BPn adlayers on Au(111)-(1×1). STS investigations employing a Au tip|BPn|Au(111)-(1×1) configuration in oxygen-free and water-free TMB are presented subsequently. The paper ends with a summary and conclusions.

Experimental Section

Chemicals: The 4-methyl-4′-(n-mercaptoalkyl)biphenyls CH_3–C_6H_4–C_6H_4–$(CH_2)_n$–SH, n = 3–6, BPn; Scheme 1 shows two examples were prepared by a Grignard C–C coupling reaction of the corresponding phenyl- or alkylbromides, followed by the conversion of the bromide to the thiol group with thiourea.[47]

The electrolyte solutions were prepared with Milli-Q water (18 MΩ, 2 ppb TOC), HCl (Merck, suprapure) and $CaCl_2$ (Aldrich, pro analysis). Absolute ethanol (KMF 08-205) and 1,3,5,-trimethylbenzene (TMB, p.a. 98%) were obtained from KMF Laborchemie Handels GmbH and Sigma–Aldrich, respectively.

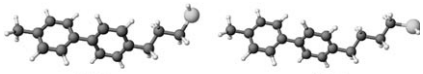

Scheme 1. Models of 4-methyl-4′-(4-mercaptopropyl)biphenyl (BP3) and 4-methyl-4′-(3-mercaptobutyl)biphenyl (BP4).

Electrode and Sample Preparation: The Au(111) single crystal electrodes were discs of 2 mm in height and 10 mm in diameter, nominal miscut ≤0.1°. Island-free Au(111)-(1×1) surfaces were prepared by immersing a flame-annealed Au(111)-$(p\times\sqrt{3})$ electrode in deareated 0.05 M HCl for 20 min.[63] The electrodes were then emersed, rinsed with absolute ethanol, and dried in a stream of argon.

The organic monolayers were prepared by immersing the dry Au(111)-(1×1) electrode with the polished and oriented surface in an ethanolic solution of BPn (2 μM–100 μM). The samples were annealed in a sealed and oxygen-free stainless steel container for 12 h or 15 h at 60 °C or 90 °C. Selected samples were treated for an additional 3 h at 120 °C (see text and figure captions for specific details). Subsequently, the modified electrodes were removed from the assembly solution, rinsed with warm ethanol to dissolve physisorbed BPn molecules, and transferred into the STM cell.

STM and STS: The STM measurements were carried out at room temperature with freshly modified electrodes in TMB using a Molecular Imaging Pico SPM. The organic solvent was chosen to ensure a strict medium control, which is not possible in air because of the unavoidable presence of a thin water film either at the STM tip or, in some unfavorable cases, on top of the adlayer. The STM tips were uncoated, electrochemically etched Pt/Ir (70:30%, 0.25 mm diameter, etching solution 1 M $CaCl_2$ + 0.25 M HCl) or Au (99.999%, 0.25 mm diameter, etching solution 1:1 mixture of 30% HCl and ethanol) wires.[64] All STM measurements were carried out in a sealed container in constant current mode employing low tunneling currents i_T (10–100 pA) and bias voltages $E_{bias} = E_T - E_S$ ranging between −0.700 V and 0.700 V. E_T and E_S represent tip and substrate potentials, respectively.

The steady-state STM and STS (current–distance and current–voltage spectroscopy) experiments were carried out sequentially. Typically, we chose the following strategy: The high-resolution topographic imaging was stopped after reaching a desired xyz position. The z-piezo feedback was then switched off temporarily. Subsequently, the STS trace was recorded, after which the STM feedback was switched. Finally, the imaging continued to inspect the surface. The STM/STS experiments were carried out exclusively with etched gold tips capable of atomic resolution.

Specifically, the distance tunneling characteristics were recorded in the regime tunneling current i_T versus relative tunneling distance perpendicular to the surface (Δz). The initial position $\Delta z = 0$ was defined in the low current range (10 nA V^{-1} preamplifier) by i_T = 60 pA and $E_{bias} = -0.200$ V, and in the high current range by i_T = 3 nA, $E_{bias} = -0.200$ V (10 μA V^{-1} preamplifier), respectively. After disabling the feedback, the i_T–Δz characteristics were measured in the range of 0.01 nA ≤ i_T ≤ 100 nA or 1 nA ≤ i_T ≤ 100 μA upon approaching the surface with a rate of 2 nm s^{-1}. One thousand data points were recorded. Traces acquired in the high current range provide access to the point of contact ($G_o \approx 77$ μS), which enabled the absolute calibration of the z-distance scale.

Current–voltage characteristics i_T versus E_{bias} were obtained at a predefined xy and constant z position, the latter being fixed by $i_T = 60$ pA, $E_{bias} = -0.200$ V (low current range) or $i_T = 3$ nA, $E_{bias} = -0.200$ V (high current range). After disabling the feedback, the bias voltage was scanned with 2 V s^{-1} either towards negative or positive values up to the predefined limits, and then back to the initial settings. One complete i_T versus E_{bias} trace was constructed from these two half cycles. A constant value of the tunneling current before and after completion of the bias voltage sweep was chosen as the criterion for selecting reliable traces.

2. Results

2.1. STM Measurements

The steady-state structures of high-coverage BP*n* monolayers ($n = 3$–6) on Au(111)-(1×1) assembled ex situ from ethanolic solutions at controlled atmosphere and temperature were monitored by high-resolution STM in TMB. Distinctly different results were found for BP*n* (n = odd) and BP*n* (n = even).[40–43] The two classes will be described separately in the following subchapters.

*2.1.1. Adlayers of BP*n *(n = Odd)*

Figures 1 and 2 show typical large scale and high resolution STM images of BP3 and BP5 in TMB assembled from 0.1 mM ethanolic solutions at various temperatures. Individual terraces

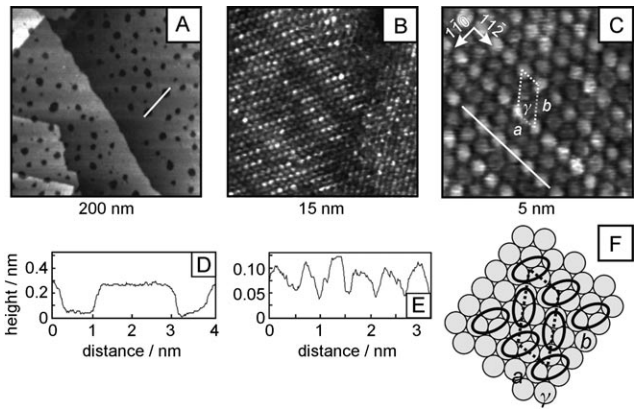

Figure 1. A) Large-scale and B) and C) high-resolution STM images of the $(\sqrt{3}\times 2\sqrt{3})$ adlayer of BP3 on Au(111)-(1×1) in TMB assembled for 12 h at 90 °C. Tunneling conditions: $E_{bias} = -0.550$ V, $i_T = 50$ pA. The unit cell is shown in (C). D) and E) Cross section apparent height profiles along the white lines in (A) and (C), respectively. F) Top view of the structure model of the $(\sqrt{3}\times 2\sqrt{3})$ overlayer of BP3 (ellipsoids) on Au(111)-(1×1) (gray circles).

are covered by large domains of a uniform adlayer. Some step edges are straight, following the main crystallographic directions of the substrate surface; others are slightly curved and buckled (Figures 1 A and 2 A II). Within the terraces, monatomic deep depressions with a typical depth of 0.25 nm were identified. These features are assigned to vacancy islands in the topmost gold layer formed during the assembly process.[10,30] We note that these substrate defects are completely covered with

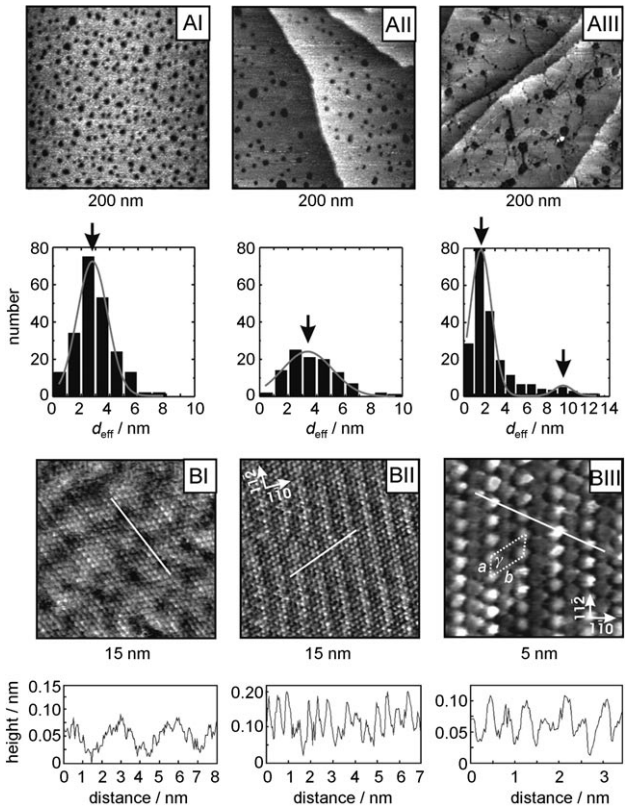

Figure 2.
A) Large-scale STM images (upper panels) of BP5 assembled on Au(111)-(1×1) at various temperatures. A I) 12 h at $T = 60$ °C; A II) 12 h at $T = 90$ °C; A III) 12 h at $T = 90$ °C and 3 h at $T = 120$ °C. Tunneling conditions: $i_T = 40$ pA, $E_{bias} = -0.600$ V. The histograms (lower panels) show the experimentally determined size distributions of the monatomic deep holes (as represented by an effective hole diameter d_{eff} assuming an approximately round shape). The solid gray lines represent the theoretical fits of a Gaussian distribution with arrows to indicate the maxima. B) Details of the STM images (upper panels) of the BP5 adlayer on Au(111)-(1×1) as obtained at two different assembly temperatures. B I) 15 h at $T = 90$ °C; B II) and B III) 15 h at 90 °C and 3 h at 120 °C. The lower panels show selected apparent height profiles along the white lines in the STM images.

organic molecules. The size and shape of the vacancy islands depend on assembly temperature and time. Figure 2 A depicts data for BP5 as a representative example. Assembly for 12 h at 60 °C gives rise to a large density of round monatomic deep vacancies of 2–3 nm in diameter. Their area percentage amounts to about 5% as estimated from a series of five representative samples. They appear evenly distributed over entire terraces (Figure 2 A I). Increasing the annealing temperature to 90 °C reduces the number of vacancies, but not their overall area. The size distribution gives a maximum around 3–4 nm diameter (Figure 1 A, Figure 2 A II). The large vacancies are not exactly round; they exhibit straight edges aligned with the [11$\bar{2}$] direction of the hexagonal substrate surface. These trends proceed at higher temperatures, such as 120 °C (Figure 2 A III). The vacancy size increases further to 9–10 nm, and the morphology of the vacancies resembles distorted hexagons. The evolution of the vacancy islands is consistent with an Ostwald ripening process.[65] The coarsening of vacancy islands is significantly accelerated at elevated temperatures, as demonstrated in Fig-

ure 2A (see also ref. [30]). However, besides the Ostwald ripening process we observed for BP5 adlayers at 120 °C (Figure 2AIII), and also for BP3 (not shown), the appearance of up to 20-nm-long chains of 1–2 nm depressions as a new feature, which pin domain boundaries of the respective BP*n* adlayer. The corresponding experimental histogram is represented by the sum of two Gaussian distributions with maxima at (1.6 ± 0.4) nm and (9.5 ± 0.5) nm. These observations may be related to the temperature-triggered relaxation of stress within the SAM.[42] We note that there is a depletion of vacancy islands in the neighborhood of steps, at the lower as well as at the upper terraces. The depletion zone increases with temperature, and extends up to 20 nm away from step edges at 120 °C.

Zooming in to smaller areas, such as illustrated in Figure 1B for BP3 adlayers assembled at 90 °C, rotational domain boundaries of 120° and other integer multiples of 60° become apparent, which indicate registry with the hexagonal substrate surface. However, these boundaries are not sharp. They exhibit a local disorder. Typical domain sizes of BP3 and BP5 adlayers range between 20 and 30 nm, often limited by surface defects such as vacancy islands. Translation domain boundaries were seldom observed. The 15-nm images, such as Figure 1B for BP3 and Figures 2BI and 2BII for BP5, reveal a hexagonal pattern of molecular-size protrusions arranged in alternating dark and bright rows. These patterns are not uniform. One observes roughly parallel dark stripes of irregular shape, which are interspaced by dark spots approximately 1 nm in diameter, giving rise to an irregular Moire-type pattern (Figure 2BI). Neighboring stripes and dark spots are separated by distances of (3.0 ± 0.5) nm. The dark areas are not related to missing molecules. Both features exhibit an apparent corrugation of 0.05 to 0.10 nm, which is higher than the geometric height difference between on-top, three-fold hollow and bridge sites,[66] thus indicating a substantial electronic contribution to the observed contrast pattern. Increasing the assembly temperature from 90 °C to 120 °C causes the nearly complete disappearance of the superstructure composed of dark rows and depressions for BP5 adlayers. On the other hand, a regular array of parallel bright stripes (apparent corrugation of 0.05–0.20 nm), which are separated by (1.7 ± 0.1) nm and aligned with the [11$\bar{2}$] direction of the substrate surface, is observed for BP5 (Figure 2BII). These temperature-dependent periodic modulations might be attributed to solitons or domain walls resulting from a structural mismatch between the molecular adlayer and the gold substrate. Duan and Garrett[67] and Cyganic et al.[42] proposed that the main path for aromatic thiole adlayers to relieve stress is by defect formation, such as a temperature-induced displacement from most favorable adsorption sites or restructuring of the top gold layer. The exact confirmation of these phenomena is beyond the precision of our STM experiments and will require high-resolution surface X-ray reflectivity studies.

High-resolution experiments with BP3 and BP5 on Au(111)-(1×1) assembled at 90 °C or 120 °C revealed rather identical details of the adlayer structures. Slightly ellipsoidal protrusions, which are assigned to individual BP*n* molecules, form a regular $(\sqrt{3}\times\sqrt{3})$R30° (R: rotation angle) sublattice. However, every other row along [11$\bar{2}$] appears brighter, independent of the imaging conditions. The corrugation alternates between 0.05 nm and 0.15 nm (Figures 1C and 2BIII). A cross section analysis confirms that the contrast variation is not accompanied by changes in the intermolecular distances, at least within the accuracy of the STM resolution.

Neglecting the long-range modulation described above, one may identify an oblique experimental unit cell with $a=(0.52\pm0.02)$ nm, $b=(1.03\pm0.05)$ nm, $\gamma=(58\pm4)°$ for BP3 and $a=(0.53\pm0.03)$ nm, $b=(0.97\pm0.08)$ nm and $\gamma=(58\pm7)°$ for BP5, both corresponding to a $(\sqrt{3}\times2\sqrt{3})$ commensurate structure with two molecules per unit cell (Table 1). The resulting area per BP3 molecule is $A_{ex}=0.23$ nm^2 ($A_{model}=0.22$ nm^2), which gives a coverage of $\Gamma_{ex}=7.3\times10^{-10}$ mol cm^{-2} ($\Gamma_{model}=7.7\times10^{-10}$ mol cm^{-2}). Similar data were obtained with BP5 (Table 1). These observations are in agreement with low energy electron diffraction (LEED) and ex situ STM experiments recently reported by Azzam et al.[39, 40a] and Cyganic et al.[40b, 41, 42] The tentative model (Figure 1F) assumes tilted BP3 (and BP5) molecules with the sulfur anchor group coordinated in threefold hollow sites of the substrate lattice (a slight misalignment exists, as indicated by the long-range modulation described above) and a herringbone-like arrangement of the elliptically shaped biphenyl moieties, thus ensuring stacking-type interactions of the parallel BP rings. Considering the spectroscopically determined tilt angle of 23° of the biphenyl group with respect to the surface normal,[47,48] an optimal molecular packing according to Ulman's concept of commensurability of intra-assembly planes is obtained .[68]

BP3 and BP5 form uniform adlayers on Au(111)-(1×1). Careful inspection of the entire surface did not reveal any additional coadsorbed structure.

2.1.2. Adlayers with BPn (n = Even)

In contrast, adlayers with BP*n*s having an even number of CH_2 units exhibit coexisting phases. Figures 3A and 4A illustrate large-scale scans of BP4 and BP6, respectively, on Au(111)-(1×1) as obtained after assembly at 90 °C. Images of BP4 revealed bright areas (α phase) and dark areas (β phase), occasionally coexisting with monatomic deep holes, which are not round but hexagonal. Step edges are facetted, typically exhibiting angles of 120° (Figure 3A). Domain boundaries between the

Table 1. Dimensions of selected unit cells of the BP*n* adlayers on Au(111)-(1×1) in mesitylene.

Molecule	*a* [nm]	*b* [nm]	γ [°]	Γ_{ex} [10^{10} mol cm^{-2}]	A_{ex} [nm^2]	Unit cell
BP3	0.52 ± 0.02	1.03 ± 0.05	58 ± 4	7.3 ± 0.3	0.23 ± 0.01	$\sqrt{3}\times2\sqrt{3}$
BP4 (α phase)	0.86 ± 0.05	2.45 ± 0.12	93 ± 5	6.3 ± 0.4	0.27 ± 0.02	$3\times5\sqrt{3}$
BP4 (β phase)	1.04 ± 0.07	2.46 ± 0.10	61 ± 4	5.9 ± 0.3	0.28 ± 0.02	$2\sqrt{3}\times5\sqrt{3}$
BP5	0.53 ± 0.03	0.97 ± 0.08	58 ± 7	7.9 ± 0.7	0.21 ± 0.02	$\sqrt{3}\times2\sqrt{3}$
BP6 (β phase)	0.97 ± 0.08	2.37 ± 0.15	59 ± 5	6.8 ± 0.4	0.25 ± 0.02	$2\sqrt{3}\times5\sqrt{3}$

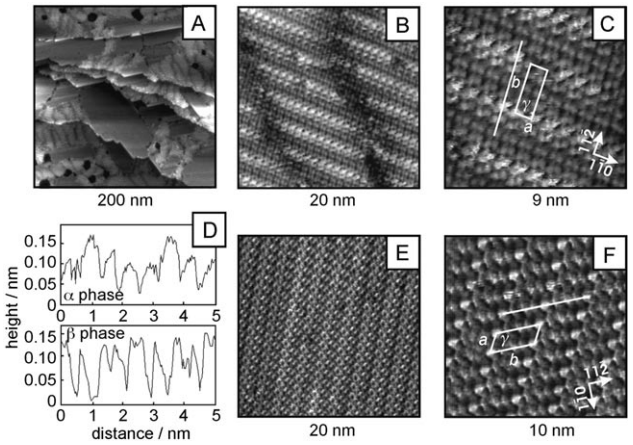

Figure 3. BP4 adlayers on Au(111)-(1×1) as obtained after assembly for 12 h at 90 °C. A) large-scale image of the coexisting α and β phases; $i_T = 70$ pA, $E_{bias} = -0.590$ V. B) and C) High-resolution images of the α phase recorded at $i_T = 44$ pA, $E_{bias} = -0.500$ V. E) and F) High-resolution images of the β phase measured at $i_T = 70$ pA, $E_{bias} = -0.550$ V. Panel (D) illustrates characteristic apparent height profiles of the α and β phases. The corresponding cross sections are indicated by the white lines in (C) and (F), respectively.

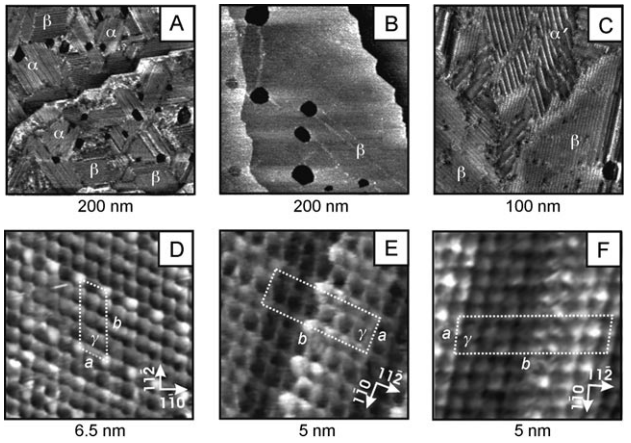

Figure 4. BP6 adlayers prepared at various temperatures on Au(111)-(1×1) in TMB. A) Coexisting α and β phases recorded after assembly for 12 h at 90 °C with $i_T = 30$ pA, $E_{bias} = -0.726$ V. B) Uniform β phase and C) coexisting β phase with an α′ phase as obtained after assembly of BP6 for 12 h at 90 °C and 3 h at 120 °C; imaging conditions: $i_T = 30$ pA, $E_{bias} = -0.700$ V. D) High-resolution image of the $(2\sqrt{3}\times5\sqrt{3})$ structure (β phase) of BP6, $i_T = 15$ pA, $E_{bias} = -0.700$ V. E) and F) High-resolution images of the compressed α′ phases $(3\times n\sqrt{3})$, $i_T = 15$ pA, $E_{bias} = -0.750$ V.

two coexisting phases are not sharp. However, no large regions of disorder exist between them.

The α phase forms small domains, seldom larger than (30×30) nm^2, which are separated by translational domain boundaries appearing somewhat darker in contrast (Figure 3B), or, less often, by rotational domain boundaries following the main symmetry directions of the Au(111)-(1×1) substrate surface. The translational boundaries exhibit a regular arrangement of dark and bright protrusions between adjacent domains. High-resolution images, such as Figure 3C, exhibit a repeating pattern composed of alternating paired rows of dark and bright contrast spots. The pattern is characterized by a quasi-rectangular unit cell with experimental dimensions $a = (0.86 \pm 0.05)$ nm along the bright rows, which are aligned with the $[1\bar{1}0]$ direction, and $b = (2.45 \pm 0.12)$ nm along the $[11\bar{2}]$ substrate direction, which enclose an angle $\gamma = (93 \pm 5)^\circ$. These dimensions are consistent with a commensurate $(3\times5\sqrt{3})$ unit cell. The cross section analysis reveals three and five protrusions, interpreted as individual BP4 molecules, of nonuniform corrugations along the two sides of the unit cell. Eight molecules per unit cell can be identified, which results in $\Gamma_{ex} = 6.3\times10^{-10}$ mol cm^{-2} ($\Gamma_{model} = 6.1\times10^{-10}$ mol cm^{-2}; Figure 5A,

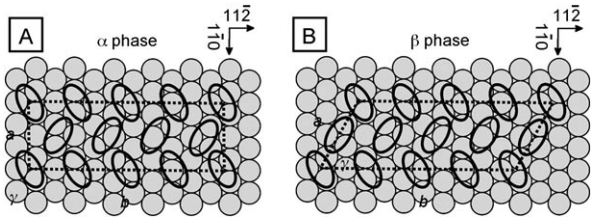

Figure 5. Top view structure models of the $(3\times5\sqrt{3})$ [α phase, (A)] and of the $(2\sqrt{3}\times5\sqrt{3})$ [β phase, (B)] structures of BP4 and BP6 SAMs on Au(111)-(1×1). The corresponding unit cells are indicated. The unit cell dimensions are summarized in Table 1.

Table 1). The nonuniform corrugation pattern, which varies systematically between 0.05 nm and 0.15 nm, suggests geometrically and electronically different adsorption sites of the individual BP4 molecules. The structure model proposed in Figure 5A assumes the adsorption of the four BP4 "corner" molecules of the unit cell, with the sulfur anchoring group coordinated to threefold hollow sites of the substrate and the remaining molecules evenly spaced along the $5\sqrt{3}$ direction of the unit cell. Within each row, the ellipsoidal BP moieties are aligned along one of the $[11\bar{2}]$ equivalent substrate directions. This arrangement alternates in a herringbone-type assembly between neighboring rows along the $[1\bar{1}0]$ direction, thus ensuring a maximum packing and in consistence with Ulman's principle of commensurability of intra-assembly planes.[68] The domain size of this α phase decreases with increasing temperature. Our structure model is identical to recently described results of Azzam et al.[40a]

The coexisting β phase (Figure 3A, areas of dark contrast) forms defect-free uniform domains, often larger than (30×30) nm^2 and rotated by 120° with respect to each other following the high-symmetry directions of the substrate surface. The domain size increases when the temperature is increased from 60 °C to 120 °C at the expense of the α phase. Zooming in to smaller areas, such as plotted in Figures 3E and F, reveals a regular arrangement of bright and dark protrusions. A repeating pattern with $a = (1.04 \pm 0.07)$ nm, $b = (2.46 \pm 0.10)$ nm and an enclosed angle $\gamma = (61 \pm 4)^\circ$ could be identified. These dimensions lead to a commensurate $(2\sqrt{3}\times5\sqrt{3})$ unit cell with the long axis aligned with the $[11\bar{2}]$ symmetry direction of the substrate. The facetted step edges observed in Figure 3A are preferentially aligned parallel to the short a axis of the unit cell. A careful analysis of cross sections along the $[11\bar{2}]$ direction gives five protrusions per $5\sqrt{3}\,a_{Au}$, which corresponds to

the long axis of the unit cell, with two typical corrugation sequences of 0.12–0.18 nm and 0.08–0.12 nm alternating between every other row. Three protrusions with an apparent corrugation height varying between 0.08 and 0.18 nm were observed per $2\sqrt{3}\,a_{Au}$ unit, that is, along the short b axis of the unit cell. Each protrusion is assigned to one BP4 molecule, which leads to eight BP4 species per unit cell and an area per molecule $A_{ex}=0.28\ nm^2$ ($A_{model}=0.27\ nm^2$). The corresponding coverage is calculated to be $\Gamma_{ex}=5.9\times10^{-10}\ mol\,cm^{-2}$ ($\Gamma_{model}=6.1\times10^{-10}\ mol\,cm^{-2}$, Figure 5B, Table 1). The systematically varying apparent corrugation heights indicate nonuniform adsorption sites. The suggested structure model is drawn in Figure 5B. Similar to the case for the α phase, we assume that the sulfur anchoring groups at the corner positions of the unit cell occupy identical lattice sites of the gold substrate, for instance threefold hollow sites, and that the remaining BP4 units are uniformly spaced in between. We further propose that the BP4 molecules align parallel along the long axis of the unit cell, that is, in the [11$\bar{2}$] direction, and that the projected ellipsoidal BP moieties in every parallel row are alternatingly rotated by $+30^\circ$ and -30° with respect to the [1$\bar{1}$0] substrate direction. This herringbone-type assembly is consistent with a 45° tilt angle of the BP4 unit to the surface normal[40,47] and enables an interdigitated packing arrangement of the alkyl chains as well as of the aromatic plane according to Ulman's commensurability concept.[68] The coverages of the α and of the β phases are identical; however, the positions of BP4 molecules occupying equivalent lattice sites appear to be shifted by $(5/4\sqrt{3}-\sqrt{3})\,a_{Au}=0.125$ nm along [11$\bar{2}$] within every other row.

BP6 forms more complex adlayers on Au(111)-(1×1) than BP4 (Figure 4). Annealing for 12 h at 90 °C results in anisotropic domains of the β phase [unit cell: $(2\sqrt{3}\times5\sqrt{3})$, Figures 4D and 5B] up to 50 nm long and 20 nm wide coexisting with the α phase [unit cell: $(3\times5\sqrt{3})$]. The α phase of BP6 appears not to be uniform. Typically, one observes rotated domains following the main symmetry directions of the hexagonal substrate. Translational domain boundaries were seldom found. Step edges are facetted, typically with angles of 120°. Often, the steps are aligned along the short direction ($2\sqrt{3}$ or 3) of the unit cell of the corresponding adlayer phase. The structure-determining role of the BP6 adlayers on the substrate morphology is also seen in the morphology of the vacancy islands, which are not round but rather hexagonal and have edges aligned with the symmetry directions of the adlayers.

Increasing the annealing temperature to 120 °C causes the growth of domains of the β phase at the expense of a new α'-type phase. Entire terraces are covered by a uniform $(2\sqrt{3}\times5\sqrt{3})$ adlayer separated by facetted and aligned steps (Figure 4B), which exhibit a few rather large hexagonal vacancy islands (10–25 nm average cross section diameter). Occasionally, one observes regions with smaller domains of the α' phase (Figure 4C). High-resolution images (Figures 4E F), exhibit rectangular $(3\times p\sqrt{3})$ unit cells ($p\geq5$) with the short axis aligned with the [1$\bar{1}$0] (or equivalent) substrate direction. Cross section profiles indicate nonequivalent corrugation heights of the protrusions, which are assigned to individual BP6 molecules within the corresponding unit cells. These observations point to different adsorption sites. The α' phases, as exemplified in Figures 4E and F, represent $(3\times6\sqrt{3})$ and $(3\times8\sqrt{3})$ structures with 12 and 18 BP6 molecules, respectively, per unit cell. Compared to the $(3\times5\sqrt{3})$ phase of BP6 at 90 °C, the more complex α' phases represent a compression of the adlayers of up to 8%, which might be related to the reduction of stress within the rigid organic layer. This stress reduction is caused by a substantial lattice mismatch.[42] Unfortunately, we could not detect clear trends in the evolution of the various α phases, which might have allowed a quantitative evaluation of this phenomenon.

2.2. Scanning Tunneling Spectroscopy

2.2.1. Distance Tunneling Characteristics

The electronic characteristics of the BP*n* self-assembled monolayers were studied by recording current–distance and current–voltage characteristics in TMB employing a gold STM tip | BP*n* | Au(111)-(1×1) configuration. Immediately after recording a STS spectrum, we monitored high-resolution STM images to ensure the structural integrity of the SAMs underneath the tip. The STS experiments were carried out on large and defect-free domains of the respective BP*n* adlayers. Great care was taken ensuring that the total thermal drift in x, y, and z directions was less than 0.01–0.02 nm s^{-1}.

Figures 6 and 7 show typical current–distance curves in a semilogarithmic representation recorded for $10\ pA\leq i_T\leq20\ \mu A$ for BP3 and BP4, respectively. The shapes of the curves are similar for both molecules. In addition, no significant differences were found for the α and the β phases of BP4. The large range of the tip current could not be measured with an acceptable signal-to-noise ratio using only a single tip current preamplifier module. Therefore, the current–distance plots shown were obtained by the superposition of two i_T–Δz measurements in different ranges, which overlap for at least one order of magnitude in tip current. The data plotted in Figures 6 and 7 represent the average of 50 approaching traces for each molecule. For illustration, selected individual curves of the low current range, $10\ pA<i_T\leq100\ nA$ (Figure 6A, BP3) and of the high current range, $3\ nA\leq i_T\leq10\ \mu A$ (Figure 7A, BP4), are shown as insets. The tunneling current i_T increases with decreasing distance between the Au tip and the Au(111)-(1×1) surface. The entire plot $\log(i_T)$ versus Δz is not linear. Three linear regions labeled I, II and III could be identified. The linear regions are slightly different for BP3 and BP4 (in parenthesis): I) $i_T<100\ pA$ ($i_T<100\ pA$); II) $200\ pA\leq i_T<200\ nA$ ($200\ pA\leq i_T<5\ \mu A$); III) $i_T>600\ nA$ ($i_T>5\ \mu A$). Individual i_T–Δz approaching curves exhibit small but characteristic current steps at $i_T\geq5\ \mu A$, which are accompanied by the evolution of current plateaus with values ranging between 10 and 20 μA for $E_{bias}=-0.200$ V (The dotted blue lines in the upper left of Figures 6 and 7 represent the average height of the first current plateau.). The occurrence of these steps is not exactly reproducible. One typically observes a scatter of 0.5 nm within the relative distance scale Δz. STM images recorded immediately after one i_T–Δz trace in the high current range demonstrate the formation of

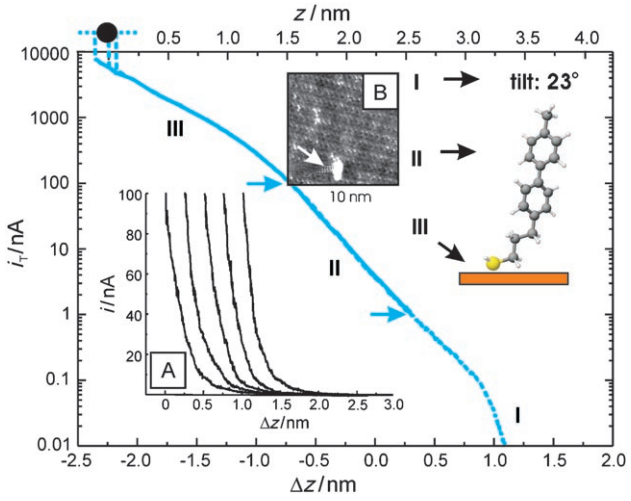

Figure 6. Current–distance curve for the $(\sqrt{3}\times2\sqrt{3})$ adlayer of BP3 on Au-(111)-(1×1) in a semilogarithmic representation. The whole plot is obtained by superposition of two sets of i_T–Δz measurements carried out in the ranges 10 pA $\leq i_T \leq$ 100 nA (dotted blue line) and 3 nA $\leq i_T \leq$ 20 μA (solid blue line). The blue arrows indicate the overlapping region. The relative distance scale Δz was chosen by defining $\Delta z = 0$ at $i_T = 3$ nA and $E_{bias} = -0.200$ V. A total of 50 individual approaching curves were averaged. The position of quantum point contact is marked by the black dot. The i_T–Δz traces are discontinuous upon approaching quantum point contact and do not allow an exact averaging in this region. The linear regions of the curve, marked I, II, and III correspond to the indicated areas of the gold STM tip | BP*n* | Au(111)-(1×1) system (see text for details). The inset (A) shows, as examples, selected individual curves measured in the low current range. The traces are shifted along the Δz axis for clarity. The inset (B) represents an image of the $(\sqrt{3}\times2\sqrt{3})$ BP3 adlayer recorded immediately after an individual i_T–Δz trace in the high current range leading to direct contact between the gold STM tip and the adsorbate-modified Au(111)-(1×1) surface. The white arrow marks the formation of a monatomic high gold island.

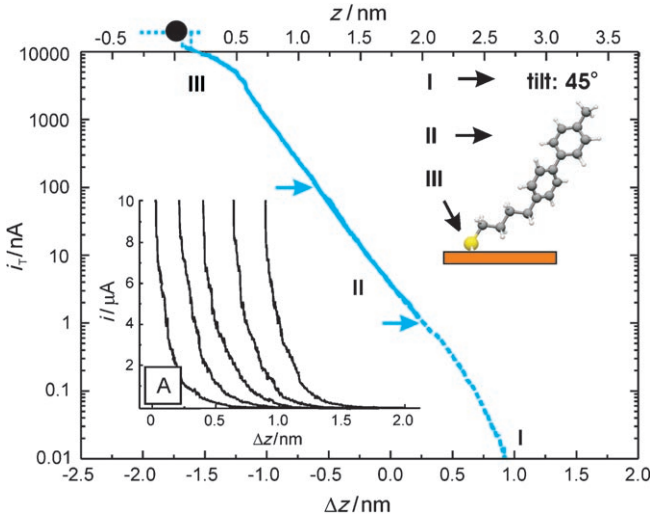

Figure 7. Current–distance curve for the $(2\sqrt{3}\times5\sqrt{3})$ overlayer of BP4 on Au(111)-(1×1) in a semilogarithmic representation. The whole plot is obtained by superposition of two sets of i_T–Δz measurements carried out in the ranges 10 pA $\leq i_T \leq$ 100 nA (dotted blue line) and 3 nA $\leq i_T \leq$ 20 μA (solid blue line). The blue arrows indicate the overlapping region. A total of 50 individual approaching curves were averaged. The position of quantum point contact is marked by the black dot. The linear regions of the curve, marked I, II, and III correspond to the indicated areas of the gold STM tip | BP*n* | Au-(111)-(1×1) system (see text for details). The inset (A) shows, as examples, selected individual curves measured in the high current range. The traces are shifted along the Δz axis for clarity.

isolated monatomic gold islands with a diameter of 1–2 nm (Figure 6, inset B). Considering a bias voltage of −0.200 V, one would expect a current of 15.6 μA for a single Au–Au atom conductance channel.[69] The experimental data are fairly close to this value. Therefore, we attribute the observations at $i_T >$ 5 μA to the formation of single Au–Au nanocontacts. Defining this point of jump-to-contact as zero distance between the tip and the substrate surface, we introduce an absolute distance scale (top *z* axis in Figures 6 and 7). The uncertainty of this calibration is estimated to be less than 0.5 nm for both systems investigated.

In an attempt to quantify the recorded current–distance characteristics, we adapt a two-layer model for coherent nonresonant electron tunneling, originally proposed by Bumm et al.[70] (Figure 8). The assumption of a nonresonant mechanism is supported by the generally accepted values of the energy differences between the HOMO and the LUMO orbitals, which are around 5 eV for the phenyl ring and 7 eV for the aliphatic alkyl chain.[25] The STM junction is assumed to be composed of two distinct layers: the solution (TMB) gap and the SAM. Each layer is characterized by a transconductance *G*, given in Equations (1) and (2):

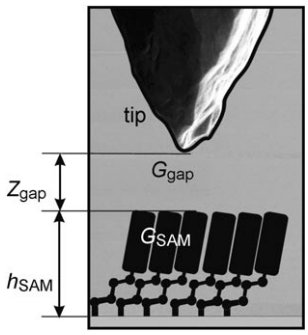

Figure 8. Two-layer tunneling junction model. The STM tunnel junction is composed of two distinct layers: the solution (TMB) gap and the BP adlayer.

$$G_{gap} = A \cdot \exp(-\alpha \cdot z_{gap}) \quad (1)$$

$$G_{SAM} = B \cdot \exp(-\beta \cdot h_{SAM}) \quad (2)$$

Where α and β are decay constants, z_{gap} and h_{SAM} are the layer thicknesses, and the prefactors *A* and *B* are the respective contact conductances. The film thickness h_{SAM} is an intrinsic property. On the basis of STM (see above and ref. [42]) and spectroscopic studies,[47] h_{SAM} is estimated to be 1.70 nm for BP3 and 1.65 nm for BP4. The solution gap thickness is controlled by the position of the STM tip. Because the transconductance is an electron tunneling probability, one obtains Equation (3) for the two-layer junction:

$$G = G_{gap} \cdot G_{SAM} = A \cdot B \cdot \exp(-\alpha \cdot z_{gap} - \beta \cdot h_{SAM}) \quad (3)$$

Equation (3) is approximated by introducing the absolute tip–distance z and an effective decay constant κ_{eff}

$$G = \text{const.} \cdot \exp(-\kappa_{eff} \cdot z). \quad (4)$$

Equation (4) reduces to h_{SAM} if $z_{gap}=0$. For $z > h_{SAM}$, the measured tunneling current depends on $(-\alpha \cdot z_{gap} - \beta \cdot h_{SAM})$ with a dominant contribution of $(-\alpha \cdot z_{gap})$ at high tunneling resistances.

The analysis of the experimental data plotted in Figures 6 and 7 for $i_T < 100$ pA (region I) leads to (10.4 ± 0.8) nm^{-1} and (9.7 ± 0.7) nm^{-1} as decay constants κ_{eff} for BP3 and BP4, respectively. We obtain, based on the Wentzel–Kramer–Brillouin approximation and assuming a rectangular tunneling barrier between two identical electrodes,[71] effective barrier heights ϕ_{eff} of (1.05 ± 0.15) eV and (0.92 ± 0.12) eV for BP3 and BP4, respectively. Referencing to the absolute distance scale z and comparison with the film thickness h_{SAM} indicate a weakly interacting STM tip positioned well above the organic adlayer. The effective decay constant κ_{eff} of the bare Au tip | TMB | Au(111)-(1×1) junction is then (10 ± 1) nm^{-1}. This value is slightly higher than for the BP*n*-modified substrate surface, indicating that tunneling in region I is dominated by the solution gap.

The values of κ_{eff}, as derived from the linear region II of the $\log(i_T)$ versus Δz plots, amount to (4.6 ± 0.7) nm^{-1} and (5.3 ± 0.5) nm^{-1} for BP3 and BP4, respectively. The values of the corresponding barrier heights ϕ_{eff} are (0.19 ± 0.06) eV and (0.25 ± 0.05) eV. The lower values of κ_{eff} and ϕ_{eff} in region II compared to region I indicate a higher transconductance of the Au tip | BP*n* | Au(111)-(1×1) junctions. Considering the absolute distance scale z (top axis in Figures 6 and 7) and the heights of the BP*n* SAMs, we conclude that strong electronic coupling exists between the tip and the sample, even before physical contact is established. In comparison to experiments carried out under UHV conditions, we did not observe a sudden change in the slope of the $\log(i_T)$ versus Δz characteristics upon formation of a contact between the STM and the SAM.[30,72] The surrounding aromatic solvent is proposed to act as a mediator at short distances. The STM tip moves from its initial z position at $\Delta z = 0$ (region I) towards the substrate surface at a fixed bias until it penetrates into the organic adlayer. Under those conditions, z_{gap} approaches zero and the transconductance G is dominated by the contribution of G_{SAM}. The values of κ_{eff} for BP3 and BP4 in region II, as estimated herein, are within the range $4\ \text{nm}^{-1} \le \kappa_{eff} \le 7\ \text{nm}^{-1}$. This range is rather typical for nonresonant electron tunneling through π-bonded molecules,[24] as documented in STM and CP-AFM studies under UHV and under ambient conditions,[55,72–74] by electron transport experiments employing Hg | SAM | Ag junctions,[29] and by adlayer-confined redox couples.[75]

An additional decrease of the effective decay parameter κ_{eff} and of the corresponding barrier height is observed in the high current range (region III), just prior to the formation of Au–Au nanocontacts. We speculate that these findings are related to increasing contact forces, which cause the mechanical compression and/or distortion of the BP*n* adlayer, which in turn might lead to the local destruction of the SAM.[76,77] Higher compression forces may also cause a significant decrease of the barrier for direct (through space) tip–sample tunneling, which opens an additional electron transport channel.[78]

Region III is more pronouncedly developed for the slightly thicker and more densely packed (25 %) BP3 adlayer compared to BP4. The tilt angle of the biphenyl moiety relative to the surface normal is significantly smaller for BP3. This property is also reflected in the observation that, in constant current mode and at a fixed bias potential, the absolute tip–substrate distance z appears to be slightly larger in the presence of BP3. As an example, we estimate z(BP3) ≈ 2.3 nm (Figure 6) and z-(BP4) ≈ 1.8 nm (Figure 7) for $i_T = 3$ nA and $E_{bias} = -0.20$ V.

2.2.2. Current–Bias Voltage Characteristics

On the basis of measurements of the distance–tunneling characteristics described above, we carried out a systematic series of current–bias voltage experiments employing long-range ordered BP3 (Figure 9) and BP4 (Figure 10) adlayers. Two distinct starting conditions were chosen: 1) The Au tip was positioned above the organic monolayer to ensure weak interactions (re-

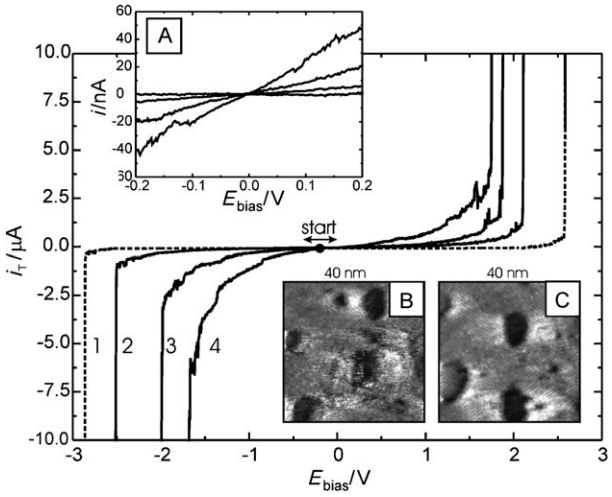

Figure 9. Current–voltage curves of the $(\sqrt{3}\times2\sqrt{3})$ adlayer of BP3 on Au-(111)-(1×1) in TMB recorded at various vertical positions of the Au STM tip. Each plotted curve represents the average of more than 20 individual traces. The curves are composed of a negative and a positive bias voltage scan (scan rate 2 V s^{-1}), which always started after equilibration of the junction at $E_{bias} = -0.200$ V and at a present tunneling current $i_{T,0}$: 1) tip positioned outside the BP3 adlayer with $i_T = 60$ pA (dashed line, recorded with a custom-designed dual preamplifier, which covered the entire current range[82]). 2)–4) tip positioned in contact with or penetrating into the adlayer with $i_T = 3$ nA, and subsequently moving the tip closer to the adlayer by 0 nm (2), 0.3 nm (3) and 0.6 nm (4) before the voltage scan was activated. The top axis of the current–distance characteristics shown in Figure 6 is used for a calibration of the absolute tip position. The inset (A) illustrates a magnification of the linear region of the i_T–E_{bias} curves. The panels (B) and (C) show images of the BP3 adlayer recorded immediately after a bias potential excursion close to the negative or to the positive breakdown potentials, respectively. The initial setpoint was $i_T = 3$ nA.

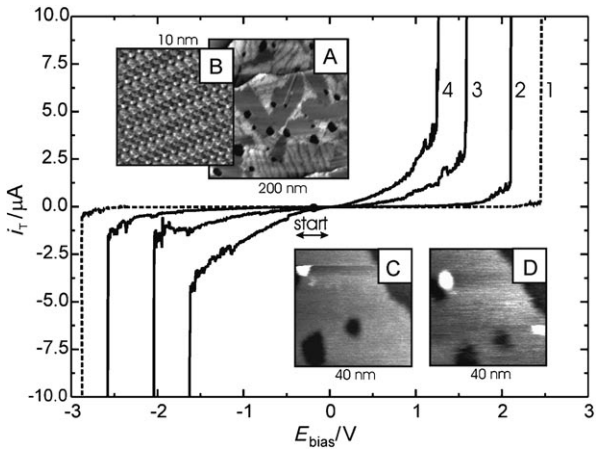

Figure 10. Current–voltage curves of the BP4 adlayer on Au(111)-(1×1) in TMB recorded at various vertical positions of the Au STM tip. The curves are composed of a negative and a positive bias voltage scan (scan rate 2 V s^{-1}), which always started after equilibration of the junction at $E_{bias} = -0.200$ V and at a present tunneling current $i_{T,0}$: 1) Tip positioned outside the BP4 adlayer with $i_{T,0} = 60$ pA (dashed line, recorded with a custom-designed dual preamplifier, which covered the entire current range[82]). 2)–4) Tip positioned in contact with or penetrating into the adlayer with $i_{T,0} = 3$ nA, and subsequently moving the tip closer towards the adlayer by 0 nm (2), 0.3 nm (3) and 0.6 nm (4). For a calibration of the absolute tip position, the top axis of the current–distance characteristics shown in Figure 7 is used. The inset (A) shows a large-scale image of the coexisting α and β phases of BP4, and (B) shows a high-resolution image of the β phase ($2\sqrt{3}\times5\sqrt{3}$) as recorded with a gold STM tip just before measuring the current–voltage characteristics. Insets (C) and (D) illustrate subsequent images of the BP4 adlayer after two consecutive excursions towards the negative breakdown potential, initial setpoint $i_T = 3$ nA.

gion I with $i_T = 60$ pA and $E_{bias} = -0.200$ V; curve 1 in Figures 9 and 10). ii) The Au tip was placed immediately in contact with or penetrating into the BP*n* adlayer, which leads to a strong electronic coupling (region II with $i_T = 3$ nA or larger and $E_{bias} = -0.200$ V, curves 2–4 in Figures 9 and 10).

The i_T–E_{bias} curves are almost symmetric and linear at low bias voltages (Figure 9 A). The estimated tunneling resistance of the Au tip | BP*n* | Au(111)-(1×1) junction follows the same trend as already discussed in the analysis of the distance tunneling characteristics (Section 2.2.1.). No evidence for coulomb blockade was found. The current increases exponentially at higher bias voltages. The experimental data can be represented qualitatively by the Simmons tunneling model[79] for $-0.500\ \text{V} \le E_{bias} \le 0.500$ V [Eq. (5)]:

$$j = \frac{6.2 \cdot 10^{-7}}{z^2}\left(\begin{array}{l}\phi_{eff} - 0.5 \cdot E_{bias} \cdot \exp(-1.025 \cdot z\sqrt{\phi_{eff} - 0.5 \cdot E_{bias}}) - \\ (\phi_{eff} + 0.5 \cdot E_{bias}) \cdot \exp(-1.025 \cdot z\sqrt{\phi_{eff} + 0.5 \cdot E_{bias}})\end{array}\right) \quad (5)$$

where z is the spacing between the electrodes or the tip–sample distance (in Å), ϕ_{eff} is an effective barrier height (in eV), and E_{bias} is the bias voltage; j represents a current density in A m^{-2}. For i_T–E_{bias} traces recorded with a setpoint in region II ($i_T = 3$ nA and $E_{bias} = -0.200$ V), one estimates values of z and ϕ_{eff} ranging from 1.5 to 2.5 nm and 0.4 eV to 0.8 eV for BP3 and BP4, respectively. These values for ϕ_{eff} are somewhat higher than those extracted from i_T–Δz characteristics. The results of z are in reasonable agreement with the proposed absolute distance scale (Figures 6 and 7). Unfortunately, we did not succeed in obtaining a unique quantitative fit because of the limited bias potential range (see below) and the uncertainties in estimating the exact current densities j.

Systematic deviations occur at higher bias voltages. All i_T–E_{bias} traces exhibit a distinct asymmetry. This effect can be attributed to the intrinsic asymmetry of the BP*n* molecules as well as to an unequal coupling in the STM junction (weak coupling between the STM tip and BP*n*; strong coupling between Au(111) and BP*n* due to chemisorption).[80]

The discontinuous decrease (increase) of the tunneling current at large negative (positive) bias potentials corresponds to the dielectric breakdown of the BP*n* adlayers.[30,76,77,81] We have imaged the respective SAMs before, during (the x–y scan was briefly interrupted for the acquisition of the spectroscopic trace, which typically took less than 2 s) and immediately after the i_T–E_{bias} measurements in order to explore the mechanism of this process (insets in Figures 9 and 10). The topographic studies were carried out in constant current mode choosing a setpoint current of 60 pA, for example; the Au tip is positioned above the BP*n* SAM. Satisfactory images could still be recorded up to 5 nA. However, stronger tip–sample interactions because of tip penetration into the organic monolayer caused a significant increase of the noise level.

The combined STM and STS measurements revealed no changes of the BP3 and BP4 adlayer structures if the bias potential sweep was restricted to values 0.500 V below (or above) the critical breakdown potentials (BDP). Excursion to higher absolute values leads to streaky images and irreversible changes of the adlayer. Upon reaching the positive or negative BDP one observes locally, for example, within the adlayer region polarized by the near field of the STM tip, dark depressions and occasionally small monatomic high gold islands (insets in Figures 9 and 10). These features point to a mechanism of field-induced dissociation and desorption.[30] The absolute values $|E_{bias}|$ of the negative BDP are higher than the corresponding positive ones, which reflects the asymmetry of the STM junction. Decreasing the tip–sample distance leads to a systematic decrease of the absolute values of the negative and positive BDP. This trend is rationalized by the local perturbation of the 2D long-range order of the adlayer upon tip penetration. On the basis of the experimentally accessible breakdown potentials and the absolute tip–sample distance, which is obtained from i_T–Δz (z) experiments (Figures 6 and 7), we estimated the electric field strength of the dielectric breakdown. Essentially independent of the initial tip position (region I or region II with $i_T \le 5$ nA), we obtained $-(0.95\pm0.05)\times10^9$ V m^{-1} and $(0.85\pm0.05)\times10^9$ V m^{-1} for the negative and positive branch, respectively, of the i_T–E_{bias} plot of BP3. The corresponding values for BP4 are $-(1.5\pm0.1)\times10^9$ V m^{-1} and $(1.2\pm0.1)\times10^9$ V m^{-1}. The higher dielectric stability of the BP4 adlayer upon polarization might be related to the larger tilt angle of the biphenyl moiety with respect to the surface normal (45°), which leads to less efficient coupling of the molecular adlayer to the applied electric

field. This interpretation is supported by a comparison with aliphatic alkanthioles. A critical threshold electric field strength of approximately $2\times10^9\,V\,m^{-1}$ was reported on the basis of different experimental approaches, such as STM,[30] CP-AFM[77] and Hg|SAM|Ag junctions.[81] The values for the electrically insulating aliphatic molecules are higher than those estimated herein.

3. Conclusions

1) 4-Methyl-4′-(*n*-mercaptoalkyl)biphenyl (CH_3–C_6H_4–C_6H_4–$(CH_2)_n$–SH, $n=3$–6, BP*n*) monolayers assembled on unreconstructed Au(111)-(1×1) surfaces at various temperatures and in the strict absence of oxygen were studied by STM and STS in 1,3,5-trimethylbenzene.

2) Annealing of the BP*n* adlayers at higher temperatures (up to 120 °C) leads to an increasing domain size and to a decreasing number density of vacancy islands due to Ostwald ripening and coarsening. Depletion of these vacancy islands was observed in the neighborhood of step edges. Temperature-induced relaxation of stress within the adlayers, especially at 120 °C, produces chains of 1 to 2 nm depressions as a new feature.

3) The high-resolution STM images reveal that BP*n* with $n=$ 3 or 5 form a $(\sqrt{3}\times2\sqrt{3})$ repeating motif. However, this pattern of molecular-sized protrusions arranged in alternating dark and bright rows is not uniform. In addition, after assembly at 90 °C, one observes dark stripes of irregular shape, which are interspaced by dark spots approximately 1 nm in diameter. Neighboring stripes and dark spots are separated by an average distance of (3.0±0.5) nm. This pattern transforms upon assembly at 120 °C into a regular array of parallel bright stripes separated by (1.7±0.5) nm.

4) More complex adlayers of coexisting structures, which depend on assembly temperature and time, were found for BP*n* with $n=4$ and 6 on Au(111)-(1×1). BP4 and BP6 form a majority $(2\sqrt{3}\times5\sqrt{3})$ phase (β phase) within the entire temperature range studied. Coexistence with a minority $(3\times5\sqrt{3})$ phase (α phase) was observed for BP4. The coexisting adlayers of BP6 are more complex. The α phase $(3\times5\sqrt{3})$, detected after assembly at 60 °C and 90 °C, compresses upon assembly at 120 °C into several rectangular $(3\times p\sqrt{3})$, $p>5$ repeat motifs.

5) The electronic characteristics of BP3 and BP4 self-assembled monolayers were studied by monitoring current–distance and current–voltage characteristics in TMB employing a gold STM tip|BP*n*|Au(111)-(1×1) configuration. Simultaneously, the structural integrity of the SAMs underneath the tip was monitored by acquiring high-resolution STM images.

6) Current–distance curves were analyzed in the current range $10\,pA\le i_T\le20\,\mu A$. The semilogarithmic $\log(i_T)$ versus Δz plots were not linear. Three limiting linear regions could be identified. Region I ($i_T<100$ pA) is assigned to a weakly interacting Au STM tip positioned above the organic adlayer. We estimated effective decay constants $\kappa_{eff}=(10.4\pm0.8)\,nm^{-1}$ and $(9.7\pm0.7)\,nm^{-1}$ for BP3 and BP4, respectively with corresponding effective barrier heights of (1.05±0.15) eV and (0.92±0.12) eV. Region II, which extends for BP3 up to 500 nA and for BP4 up to 5 μA, corresponds to a strong electronic coupling between the tip and the adlayer with the gold tip penetrating into the adlayer. The values of κ_{eff} vary between 4.6 and $5.3\,nm^{-1}$, which leads to effective barrier heights of 0.19 to 0.25 eV. The lower values of κ_{eff} and ϕ_{eff} in region II as compared to region I indicate a higher transconductance of the Au tip|BP*n*|Au(111)-(1×1) junctions. An additional decrease of the effective decay parameter κ_{eff} and of the corresponding barrier height is observed in the high current range (region III), just prior to the formation of Au–Au nanocontacts. We speculate that these findings are related to increasing contact forces, which cause the mechanical compression and/or distortion of the BP*n* adlayer.

7) Current–bias voltage characteristics were recorded employing long-range ordered BP3 and BP4 adlayers. Two distinct starting conditions were chosen: i) The Au tip was positioned above the organic monolayer (region I), and ii) the Au tip was placed immediately in contact with or penetrating into the BP*n* adlayer (region II). The i_T–E_{bias} curves are almost symmetric and linear at low bias voltages. The experimental data can be qualitatively represented by the Simmons tunneling model for $-0.500\,V\le E_{bias}\le0.500\,V$. The traces exhibit a distinct asymmetry at higher values of E_{bias}. The origin of the asymmetry is attributed to the intrinsic asymmetry of the BP*n* molecules and to an unequal coupling in the STM junction (weak coupling between the STM tip and BP*n*; strong coupling between Au(111) and BP*n* due to chemisorption).

8) The adlayers are modified upon reaching the negative or positive critical breakdown potentials. Considering the absolute tip–sample distance, we estimated the electric field strength of the dielectric breakdown. Independent of the initial tip position (region I or region II), we obtained $-(0.95\pm0.05)\times10^9\,V\,m^{-1}$ and $(0.85\pm0.05)\times10^9\,V\,m^{-1}$ for the negative and positive branches, respective, of the i_T–E_{bias} plot for BP3. The corresponding values for BP4 amount to $-(1.5\pm0.1)\times10^9\,V\,m^{-1}$ and $(1.2\pm0.1)\times10^9\,V\,m^{-1}$. The higher dielectric stability of the BP4 adlayer upon polarization might be related to the large tilt angle of the biphenyl moiety with respect to the surface normal (45°). The values for biphenyl-type derivatives estimated in this study are lower than those reported for electrically insulating aliphatic alkanethiols.

Finally, the stability range of the BP*n* adlayers on Au(111)-(1×1) in TMB upon bias polarization can be as high as 5 V if the probing STM tip is positioned outside the SAM. Decreasing the tip–sample distance leads to a smaller stability range of the adlayer.

Acknowledgements

G.J.S. was supported by an Alexander von Humboldt Research Fellowship. R.A.S. and I.P. acknowledge support from the German Academic Exchange Agency. The work of M.H., U.S. and Th.W. was supported by the Institute of Functional Materials for Information Technology (IFMIT), the RWTH Aachen and the Research Center Jülich. We also acknowledge the help of J. Kiesgen and B. Hahn in synthesizing the BP*n* derivatives. The authors also like to thank M. Buck for valuable comments.

Keywords: monolayers · *n*-(mercaptoalkyl)biphenyls · scanning probe microscopy · self-assembly · surface chemistry

[1] *Encyclopedia of Nanoscience and Nanotechnolgy* (Ed.: H. S. Nalwa), American Scientific, Valencia, **2004**.
[2] J. M. Lehn, *Supramolecular Chemistry*, VCH, Weinheim, **1995**.
[3] A. C. Templeton, W. P. Wuellfing, R. W. Murray, *Acc. Chem. Res.* **2000**, *33*, 27.
[4] J. H. Fendler, *Chem. Mater.* **2001**, *13*, 3196.
[5] W. C. Bigelow, D. L. Pickett, W. A. Zisman, *J. Colloid Sci.* **1946**, *1*, 513.
[6] A. Ulman, *Chem. Rev.* **1996**, *96*, 1533.
[7] A. Ulman, *Acc. Chem. Res.* **2001**, *34*, 855.
[8] J. Sagiv, *J. Am. Chem. Soc.* **1980**, *102*, 92.
[9] R. G. Nuzzo, D. L. Allara, *J. Am. Chem. Soc.* **1983**, *105*, 4481.
[10] G. E. Poirier, *Chem. Rev.* **1997**, *97*, 1117.
[11] F. Schreiber, *J. Phys. Condens. Matter* **2004**, *16*, R881.
[12] R. K. Smith, P. A. Lewis, P. S. Weiss, *Prog. Surf. Sci.* **2004**, *75*, 1.
[13] J. C. Love, L. A. Estroff, J. K. Kribel, R. G. Nuzzo, G. M. Whitesides, *Chem. Rev.* **2005**, *105*, 1103.
[14] M. Mrksich, C. S. Chen, Y. N. Xia, L. E. Dike, D. E. Ingber, G. M. Whitesies, *Proc. Natl. Acad. Sci. USA* **1996**, *93*, 10775.
[15] H. S. Ahn, P. D. Cuong, S. Park, Y. W. Kim, J. C. Lim, *Wear* **2003**, *255*, 819.
[16] R. D. Piner, J. Zhu, F. Xu, S. H. Hong, C. A. Mirkin, *Science* **1999**, *283*, 661.
[17] S. Flink, F. C. J. M. van Neggel, D. N. Renhoundt, *Adv. Mater.* **2000**, *12*, 1315.
[18] C. M. Whelan, M. Kinsella, H. M. Ho, K. Maex, *J. Electrochem. Soc.* **2004**, *151*, B33.
[19] H. O. Finklea in *Electroanal. Chem., Vol. 19* (Eds.: A. J. Bard, M. Dekker) New York, **1996**, p. 109.
[20] T. Baunach, V. Ivanova, D. M. Kolb, H. G. Boyen, P. Ziemann, M. Büttner, P. Oelhafen, *Adv. Mater.* **2004**, *16*, 2024.
[21] B. A. Mantooth, P. S. Weiss, *Proc. IEEE* **2003**, *91*, 1785.
[22] *Introduction to Molecular Electronics* (Eds.: G. Cuniberti, G. Fagas, K. Richter), Springer, Heidelberg, **2005**.
[23] *Molecular Wires and Nanoscale Conductors—Fundamentals and Applications*, *Faraday Discuss. Vol. 131,* **2006**.
[24] A. Salomon, D. Cahen, S. M. Lindsay, J. Tomfohr, V. B. Engelkes, C. D. Frisbie, *Adv. Mater.* **2003**, *15*, 1881.
[25] R. L. McCreery, *Chem. Mater.* **2004**, *16*, 4477.
[26] C. E. D. Chidsey, *Science* **1991**, *251*, 919.
[27] A. M. Becka, C. J. Miller, *J. Phys Chem.* **1992**, *96*, 2657.
[28] H. O. Finklea, D. D. Handshew, *J. Am. Chem. Soc.* **1992**, *114*, 3173.
[29] R. E. Holmlin, R. Haag, M. L. Chabinyc, R. F. Ismagilov, A. E. Cohen, A. E. Terfort, M. A. Rampi, G. M. Whitesides, *J. Am. Chem. Soc.* **2001**, *123*, 5075.
[30] G. Yang, G. Liu, *J. Phys. Chem. B* **2003**, *107*, 8746.
[31] X. Li, J. He, J. Hihath, B. Q. Xu, S. M. Lindsay, N. J. Tao, *J. Am. Chem. Soc.* **2006**, *128*, 2135.
[32] E. Sabatani, J. Cohen-Boulakia, M. Bruening, I. Rubinstein, *Langmuir* **1993**, *9*, 2974.
[33] H. D. Sikes, J. F. Smalley, S. P. Dudek, A. R. Cook, M. D. Newton, C. E. D. Chidsey, S. W. Feldberg, *Science* **2001**, *291*, 1519.
[34] P. Cyganik, M. Buck, W. Azzam, Ch. Wöll, *J. Phys. Chem. B* **2004**, *108*, 4989.
[35] L. A. Bumm, J. J. Arnold, M. T. Cygan, T. D. Dunbar, T. P. Burgin, L. Jones, D. L. Allara, J. M. Tour, P. S. Weiss, *Science* **1996**, *271*, 1705.
[36] M. A. Reed, C. Zhou, C. J. Muller, T. P. Burgin, J. M. Tour, *Science* **1997**, *278*, 252.
[37] D. M. Adams, L. Brus, C. E. D. Chidsey, S. Creager, C. Creutz, C. R. Kagan, P. V. Kamat, M. Lieberman, S. Lindsay, R. A. Marcus, R. M. Metzger, M. E. Michel-Beyerle, J. R. Miller, M. D. Newton, D. R. Rollison, O. Sankey, K. S. Schanze, J. Yardely, X. Zhu, *J. Phys. Chem. B* **2003**, *107*, 6668.
[38] J. F. Kang, A. Ulman, S. Liao, R. Jordan, G. Yang, G. Liu, *Langmuir* **2001**, *17*, 95.
[39] W. Azzam, C. Fuxen, A. Birkner, H. T. Rong, M. Buck, Ch. Wöll, *Langmuir* **2003**, *19*, 4958.
[40] a) W. Azzam, P. Cyganik, G. Witte, M. Buck, Ch. Wöll, *Langmuir* **2003**, *19*, 8262; b) P. Cyganik, M. Buck, *J. Am. Chem. Soc.* **2004**, *126*, 5960.
[41] P. Cyganik, M. Buck, W. Azzam, Ch. Wöll, *J. Phys. Chem. B* **2004**, *108*, 4989.
[42] P. Cyganik, M. Buck, J. D. E. T. Wilton-Ely, Ch. Wöll, *J. Phys. Chem. B* **2005**, *109*, 10902.
[43] R. Aguilar-Sanchez, G. J. Su, M. Homberger, U. Simon, Th. Wandlowski, unpublished results.
[44] T. Ishida, W. Mizutani, N. Choi, U. Akiba, M. Fujihara, H. Tokumoto, *J. Phys. Chem. B* **2000**, *104*, 11680.
[45] C. Fuxen, W. Azzam, R. Arnold, G. Witte, A. Terfort, Ch. Wöll, *Langmuir* **2001**, *17*, 3689.
[46] W. Azzam, A. Bashir, A. Terford, T. Stronskus, Ch. Wöll, *Langmuir* **2006**, *22*, 3647.
[47] H. T. Rong, S. Frey, Y. J. Yang, M. Zharnikov, M. Buck, M. Wühn, Ch. Wöll, G. Helmchen, *Langmuir* **2001**, *17*, 1582.
[48] K. Heister, H. T. Rong, M. Buck, M. Zharnikov, M. Grunze, L. S. O. Johanson, *J. Phys. Chem. B* **2001**, *105*, 6888.
[49] A. Shaporenko, M. Brunnbauer, A. Terfort, M. Grunze, M. Zharnikov, *J. Phys. Chem. B* **2004**, *108*, 14462.
[50] S. Datta, W. Tian, S. H. Hong, R. Reifenberger, J. I. Henderson, C. P. Kubiak, *Phys. Rev. Lett.* **1997**, *79*, 2530.
[51] Z. Donhauser, B. A. Mantooth, K. F. Kelley, L. A. Bumm, J. D. Monnell, J. J. Stapleton, D. W. Price, D. L. Allara, J. M. Tour, P. S. Weiss, *Science* **2001**, *292*, 2303.
[52] X. Xiao, L. A. Nagahara, A. M. Rawlett, N. J. Tao, *J. Am. Chem. Soc.* **2005**, *127*, 9235.
[53] G. Dholakia, W. Fan, M. Meyyappan, *Appl. Phys. A* **2005**, *80*, 1215.
[54] Z. Li, B. Han, G. Meszaros, I. Pobelov, Th. Wandlowski, A. Blaszcyk, M. Mayor, *Faraday Discuss.* **2006**, *131*, 121.
[55] D. J. Wold, R. Haag, M. A. Rampi, C. D. Frisbie, *J. Phys. Chem. B* **2002**, *106*, 2813.
[56] a) A. M. Rawlett, T. J. Hopson, L. A. Nagahara, R. K. Tsui, G. K. Ramachandran, S. M. Lindsay, *Appl. Phys. Lett.* **2002**, *81*, 3043; b) X. D. Cui, A. Primak, X. Zarate, J. Tomfohr, O. F. Sankey, A. L. Moore, T. A. Moore, D. Gust, G. Harris, S. M. Lindsay, *Science* **2001**, *294*, 571; c) X. D. Cui, X. Zarate, J. Tomfohr, O. F. Sankey, A. Primak, A. L. Moore, T. A. Moore, D. Gust, G. Harris, S. M. Lindsay, *Nanotechnology* **2002**, *13*, 5.
[57] F.-R. F. Fan, J. Yang, L. Cai, D. W. Price, S. M. Dirk, D. V. Kosynkin, Y. Yao, A. M. Rawlett, J. M. Tour, A. J. Bard, *J. Am. Chem. Soc.* **2002**, *124*, 5550.
[58] J. Chen, M. A. Reed, A. M. Rawlett, J. M. Tour, *Science* **1999**, *286*, 1550.
[59] J. G. Kushmerick, D. B. Holt, J. C. Yang, J. Narici, M. H. Moore, R. Shashiidhar, *Phys. Rev. Lett.* **2002**, *89*, 086801.
[60] H. S. J. Van der Zant, Y. V. Kervennic, M. Poot, K. O'Neill, Z. de Groot, J. M. Thijssen, H. B. Heersche, N. Stuhr-Hansen, T. Bjornholm, D. Vanmaekelbergh, C. A. vanWalree, L. W. Jenneskens, *Faraday Discuss.* **2006**, *131*, 347.
[61] J. O. Lee, G. Lientschnig, F. Wiertz, M. Struijk, R. A. J. Janssen, R. Egberink, D. A. Reinhoudt, P. Hadley, C. Dekker, *Nano Lett.* **2003**, *3*, 113.
[62] J. G. Kushmerick, A. S. Blum, D. P. Long, *Anal. Chim. Acta* **2006**, *568*, 20.
[63] M. H. Hölzle, Th. Wandlowski, D. M. Kolb, *J. Electroanal. Chem.* **1995**, *394*, 271.
[64] G. Meszaros, I. Pobelov, Z. Li, Th. Wandlowski, unpublished results.
[65] O. Cavalleri, A. Hirstein, K. Kern, *Surf. Sci.* **1995**, *340*, L960.
[66] H. Kondoh, M. Iwasaki, T. Shimada, K. Amemiya, T. Yokoyama, T. Ohta, M. Shimomura, S. Kono, *Phys. Rev. Lett.* **2003**, *90*, 066102.
[67] L. Duan, S. J. Garrett, *J. Phys. Chem. B* **2001**, *105*, 9812.
[68] A. Ulman, R. P. Scaringe, *Langmuir* **1992**, *8*, 894.
[69] R. Landauer, *IBM J. Res. Dev.* **1957**, *1*, 223.
[70] L. A. Bumm, J. J. Arnold, T. D. Dunbar, D. L. Allara, P. S. Weiss, *J. Phys. Chem. B* **1999**, *103*, 8122.
[71] *Quantum Mechanics* (Ed.: A. S.Dawydov), Pergamon, Oxford, **1976**.
[72] S. Wakamatsu, S. Fuji, U. Akiba, M. Fujihira, *Ultramicroscopy* **2003**, *97*, 19.
[73] S. Wakamatsu, U. Akiba, M. Fujihira, *Jpn. J. Appl. Phys. Part 1* **2002**, *41*, 4998.
[74] B. Lüssem, L. Müller-Meskamp, S. Karthäuser, R. Waser, M. Homberger, U. Simon, *Langmuir* **2006**, *22*, 3021.
[75] S. B. Sachs, S. P. Dudek, R. P. Hsung, L. R. Sita, J. F. Smalley, M. D. Newton, S. W. Feldberg, C. E. D. Chidsey, *J. Am. Chem. Soc.* **1997**, *119*, 10563.
[76] X. D. Cui, X. Zarate, J. Tomfohr, O. F. Sankey, A. Primak, A. L. Moore, T. A. Moore, D. Gust, G. Harris, S. M. Lindsay, *Nanotechnology* **2002**, *13*, 5.
[77] D. J. Wold, C. D. Frisbie, *J. Am. Chem. Soc.* **2001**, *123*, 5549.

[78] J. J. Davis, N. Wang, A. Morgan, T. T. Zhang, J. W. Zhao, *Faraday Discuss.* **2006**, *131*, 167.
[79] J. G. Simmons, *J. Appl. Phys.* **1963**, *34*, 1793.
[80] S. Datta, W. Tian, S. H. Hong, R. Reifenberger, J. I. Henderson, C. P. Kubiak, *Phys. Rev. Lett.* **1997**, *79*, 2533.
[81] R. Haag, M. A. Rampi, R. E. Holmlin, G. M. Whitesides, *J. Am. Chem. Soc.* **1999**, *121*, 7895.
[82] G. Meszaros, C. Li, Th. Wandlowski, unpublished results.

Received: December 12, 2006

